Observations of the size distribution of frazil ice in an Ice Shelf Water plume

Eamon K Frazer[1], Patricia Jean Langhorne[1], Greg H Leonard[1], Natalie Joy Robinson[2], and Daniel Schumayer[1]

[1]University of Otago
[2]National Institute of Water and Atmospheric Research

November 22, 2022

Abstract

The size distribution of frazil ice is currently unconstrained in ice shelf cavity modeling. Here we observe the time-dependent behavior of the number and size of frazil ice particles in an Ice Shelf Water plume. A novel acoustic scattering inversion was used to infer frazil ice crystal diameters, assuming a log-normal distribution. Observation sites were on land-fast sea ice approximately 13 and 33 km from the front of the McMurdo Ice Shelf, Antarctica. The water column from the ice-water interface to 30 m below mean sea level was monitored over 3 weeks in November of 2016 and 2017. At 15 m below sea level the mean frazil crystal diameter was $\sim$\SI{1}{\milli\metre}. Fractional ice volume, derived from frazil crystal size and number density, correlates with in-situ supercooling (up to \SI{50}{\milli\kelvin} at \SI{15}{\metre} below sea level). The data presented here provide valuable input for model initiation and evaluation.

Observations of the size distribution of frazil ice in an Ice Shelf Water plume

Eamon K. Frazer[1], Pat J. Langhorne[1], Greg H. Leonard[2], Natalie J. Robinson[3], Dániel Schumayer[1,4]

[1]Department of Physics, University of Otago, Dunedin, New Zealand
[2]School of Surveying, University of Otago, Dunedin, New Zealand
[3]National Institute of Water and Atmospheric Research, Wellington, New Zealand
[4]The Dodd-Walls Centre for Photonic and Quantum Technologies, Dunedin, New Zealand

Key Points:

- Acoustic scattering-derived frazil ice populations have been observed down to 30 m in Ice Shelf Water beneath Antarctic sea ice.
- Assuming a log-normal distribution, mean frazil crystal diameter is ∼1 mm at 15 m below sea level and ∼13 km from the ice shelf front.
- Model-derived fractional ice volume correlates with in-situ supercooling of up to 50 mK at 15 m below sea level.

Corresponding author: Pat J. Langhorne, `pat.langhorne@otago.ac.nz`

Abstract

The size distribution of frazil ice is currently unconstrained in ice shelf cavity modeling. Here we observe the time-dependent behavior of the number and size of frazil ice particles in an Ice Shelf Water plume. A novel acoustic scattering inversion was used to infer frazil ice crystal diameters, assuming a log-normal distribution. Observation sites were on land-fast sea ice approximately 13 and 33 km from the front of the McMurdo Ice Shelf, Antarctica. The water column from the ice-water interface to 30 m below mean sea level was monitored over 3 weeks in November of 2016 and 2017. At 15 m below sea level the mean frazil crystal diameter was $\sim$1 mm. Fractional ice volume, derived from frazil crystal size and number density, correlates with in-situ supercooling (up to 50 mK at 15 m below sea level). The data presented here provide valuable input for model initiation and evaluation.

Plain Language Summary

For the first time we have observed the number and sizes of tiny, disc-like, crystals that appear beneath the springtime sea ice of McMurdo Sound, Antarctica. They are generated by melting at the base of gigantic floating glaciers that surround the Antarctic continent, and are carried out beneath the sea ice in water that is just below its freezing point. From sonar measurements we have found that at 15 m below sea level, there is about one disc-shaped ice crystal with an average diameter of approximately 1 mm in each 10 cubic centimeters of sea water. Previously there have been no observed sizes of these ice crystals to guide modeling of the interaction between glaciers and the ocean, and our new results provide valuable input for model initiation and evaluation.

1 Introduction

Suspended frazil ice crystals form in turbulent fresh or salt water that is colder than its salinity- and pressure-dependent freezing temperature, a state referred to as in-situ supercooled (e.g., Martin, 1981; Daly, 1984; Tsang & Hanley, 1985; Schneck et al., 2019). In natural water bodies in-situ supercooling can be generated in numerous ways (Martin, 1981), but two are of particular importance in the Southern Ocean. The first is the rapid heat loss at the surface of open water, for example in a coastal polynya or a lead, often driven by high winds (e.g., Martin, 1981; Ito et al., 2015, 2020). Alternatively, supercooling may arise through a process known as the "ice pump" (Lewis & Perkin, 1986). The "ice pump" is driven by an intrusion of salty water that causes ice shelf basal melting/dissolving, thereby releasing fresh water of glacial origin at depth in the water column (MacAyeal, 1984). This mixture of colder, fresher water has relatively low density and is therefore buoyant. It rises up the basal slope of the ice shelf, becomes supercooled through the change in its pressure-dependent freezing point (Foldvik & Kvinge, 1974) and frazil crystal formation is initiated (Jenkins & Bombosch, 1995; Smedsrud & Jenkins, 2004). The supercooled water can extend beyond the front of the ice shelf and travel beneath adjacent sea ice as part of an Ice Shelf Water (ISW) plume (Robinson et al., 2014; Hughes et al., 2014). The supercooling decays with distance from the ice shelf front (Lewis & Perkin, 1985), as does the influence of the plume on the sea ice cover (Dempsey et al., 2010; Hughes et al., 2014; Langhorne et al., 2015; Brett et al., 2020).

Individual frazil ice crystals in rivers, lakes and the ocean usually begin as disc-shaped particles, evolving to more irregular shapes as they grow. Collisions cause the crystals to sinter together into groups of particles, known as frazil flocs (e.g., Martin, 1981). In rivers, mean individual frazil crystal diameters are reported between 0.1 and 6 mm (McFarlane et al., 2017), with typical fractional ice volumes in the range 10^{-3} to 10^{-6} (McFarlane et al., 2019). The mean frazil crystal diameter has been shown to follow a log-normal distribution in freshwater laboratory experiments (McFarlane et al., 2015; Schneck et al., 2019) and in rivers (McFarlane et al., 2017, 2019).

Quantitative observations of the shape and size of individual frazil ice particles in salt water of ocean salinity are sparse, with suspended ice crystal diameters ranging 1–3 mm in laboratory experiments (e.g., Martin, 1981; Smedsrud, 2001; Schneck et al., 2019) and an upper bound of 10–25 mm in the ocean (Dieckmann et al., 1986; Penrose et al., 1994; Gough et al., 2012). Only Schneck et al. (2019) have made laboratory measurements of frazil size distributions in salt water, and shown they again follow a log-normal distribution. The ice crystal diameters are $\sim$13% smaller than in fresh water, with a mean diameter of 0.45 mm, standard deviation 0.31 mm, while flocs have a mean of 1.47 mm and standard deviation of 1.28 mm (Schneck et al., 2019).

McFarlane et al. (2017, 2019) also summarize the methods of detection of suspended frazil in laboratory and river studies. The most successful methods in rivers are high resolution photography (McFarlane et al., 2017, 2019), and acoustic backscatter techniques (Marko & Jasek, 2010; Richard et al., 2011; Marko et al., 2015; Ghobrial et al., 2013). For the latter, a scattering model is needed to resolve frazil particle size from received sound, and Ghobrial et al. (2013) have used sphere, prolate spheroid, and disk models. Using multi-frequency acoustic scattering and assuming a log-normal distribution of equivalent spheres (Marko & Topham, 2015), Marko et al. (2015) have deduced suspended frazil particle size distribution in rivers. In the ocean, where the imperative is to sample a large volume, acoustic techniques have been preferred. Sonar returns (Dieckmann et al., 1986; Penrose et al., 1994; Ito et al., 2015, 2020) and Acoustic Doppler Current Profiler (ADCP) backscatter strength (Leonard et al., 2006; Ito et al., 2017, 2020) are enhanced by suspended frazil ice. Fractional ice volumes are estimated in range 10^{-7}–10^{-6} (Penrose et al., 1994; Ito et al., 2017). Thus salt water observations of the presence, shape and size of suspended frazil ice particles are very limited but laboratory studies indicate particle sizes comparable to freshwater observations (Schneck et al., 2019).

Inclusion of suspended frazil in ocean modeling is well developed (e.g., Jenkins & Bombosch, 1995; Svensson & Omstedt, 1998). Plume models include a range of frazil crystal size classes (e.g., Smedsrud & Jenkins, 2004; Holland & Feltham, 2005; Hughes et al., 2014; Rees Jones & Wells, 2018). Frazil crystal size distribution is also now included in three-dimensional ocean circulation models (Galton-Fenzi et al., 2012). In agreement with observations, modeling suggests the magnitude of the supercooling and the rate of ice crystal deposition depend strongly on distance from the ice shelf (Hughes et al., 2014). Smedsrud and Jenkins (2004) predict that typically, crystals up to $\sim$2.0 mm in diameter are kept in suspension, and concentrations reach a maximum fractional ice volume of 4.4×10^{-4}. However, model results depend upon the initial frazil crystal size distribution. To date, no measurements exist with which to initiate or validate the output of these model distributions.

In summary, there are presently no measurements of the size distribution of suspended frazil in natural ocean conditions (Schneck et al., 2019; Ito et al., 2020). In this paper we present acoustic observations acquired in 2016 and 2017 from a four-frequency acoustic sounder deployed through sea ice (see Figure 1a). Oceanographic moorings operated alongside to provide simultaneous ocean conditions. A novel acoustic scattering model developed specifically for frazil ice that considers the crystals to be oblate spheroids (Kungl et al., 2020) is used to quantify the time-dependent frazil ice populations formed by the interaction between ice shelves, the ocean and the adjacent sea ice.

2 Methods

2.1 Area Description

McMurdo Sound is an area of seasonally open water bounded by Ross Island, the Antarctic coastline, and the McMurdo Ice Shelf, which is connected to the much larger Ross Ice Shelf (Figure 1a). In McMurdo Sound, the ocean below the land-fast sea ice is seasonally supercooled by up to 45 mK (e.g., Lewis & Perkin, 1985; Leonard et al., 2011; Robinson et al., 2014). The frazil crystals in the supercooled water are driven by buoyancy to settle beneath the sea ice where they form a porous, friable sub-ice platelet layer (Leonard et al., 2006; Gough et al., 2012). This sub-ice platelet layer has been observed to be up to 8 m thick in western McMurdo Sound (Hughes et al., 2014; Langhorne et al., 2015), suggesting this location has a sustained ISW presence where suspended frazil ice crystals are likely to be observed.

2.2 Instrumentation & Data Processing

The acoustic back-scattering data were collected by an Acoustic Zooplankton Fish Profiler (AZFP, manufactured by ASL Environmental Science) utilizing four frequency channels: 125, 200, 455, and 769 kHz. The ASL Matlab Toolbox (version 1.1) was used to convert raw instrument counts to acoustic volume backscattering strength, S_v, related to the back-scattering cross section, σ_{bs}. Scattering strength, S_v, is smoothed in 11 minute spans and spatially averaged over 5 depth cells of 0.1 m thickness (Frazer, 2019; Kungl et al., 2020). Typical depth profiles are shown in Figure 1b. The operation of the AZFP is described in more detail in the Supporting Information and in Kungl et al. (2020).

Kungl et al. (2020) have determined the theoretical acoustic back-scattering cross-section of an individual oblate spheroid, $\sigma_{\mathrm{bs}}(\nu, D)$. Assuming a dilute population of such scatterers with random diameter D, the total back-scattering cross-section

$\Sigma^{\rm th}_{\rm bs}(\nu)$ relative to the intensity of the incident plane wave (referenced to 1m) can be modeled by

$$\Sigma^{\rm th}_{\rm bs}(\nu) = N \int g(D)\, \sigma_{\rm bs}(\nu, D)\, dD, \tag{1}$$

where N is the number density of scatterers, and g is the probability distribution of scatterers' diameter. Following Marko and Topham (2015) and Marko et al. (2015) and supported by recent observations (McFarlane et al., 2015, 2017, 2019; Schneck et al., 2019), we choose a log-normal distribution, $g \sim \Lambda(\mu, \sigma)$. We associate $\Sigma^{\rm th}_{\rm bs}(\nu)$ with the measured back-scattering cross-section $\Sigma^{\rm obs}_{\rm bs}(\nu)$. This fitting leads to an optimization algorithm for the yet unknown parameters, $\{\mu, \sigma, N\}$, which minimizes the sum of residual squares $R = \sum_{i=1}^{4} \left[S^{\rm th}(\nu_i) - S^{\rm obs}(\nu_i)\right]^2$. Here $S^{\rm obs} = 10\log_{10}(\Sigma^{\rm obs}_{\rm bs})$ and $S^{\rm th} = 10\log_{10}(\Sigma^{\rm th}_{\rm bs})$. The optimization is carried out at all depths and for all moments in time. A more detailed description of the data processing is available in the Supporting Information.

We have also collected complementary oceanographic data by moorings comprising a SeaGuard single-depth current meter, SeaBird Electronics SBE-56 thermistors, and SeaBird Electronics SBE-37 microCATs, which recorded current, temperature, and salinity time-series, respectively. All oceanographic data are reported here in TEOS-10 using the Gibbs function for seawater thermodynamics (Feistel, 2008), applying the scripts generated by McDougall (2011), and using the latest version of the toolbox available (www.teos-10.org/software.htm). Tidal height forecast data were produced from WWW Tide and Current Predictor for Ross Island, Antarctica.

3 Results

The observations were made at sites 33 km (November 2016) and 13 km (November 2017) from the ice shelf front (see Figure 1a) with the AZFP deployed looking upwards from a nominal depth of 30 m. Datasets coincide with significant portions of a spring/neap tidal cycles and were positioned to be within the expected path of the ISW plume emanating from the McMurdo Ice Shelf cavity (Langhorne et al., 2015). At times, especially during the 2017 deployment, the AZFP drifted upwards through the water column due to buoyant forces from ice accumulation on the instrument and rope. In Figure 1c and d, this is accounted for by using the on-board pressure sensor to determine the AZFP's vertical position in the water column, and adjusting the range bins appropriately. The AZFP was therefore hauled out of the water to remove ice deposition, and was redeployed within a day. Thus there are two (effectively) continuous time-series of acoustic back-scattering in each year for a total of four uninterrupted deployments of 3–7 days each. The times of all observations are reported in NZST.

The site of the oceanographic mooring was approximately 100 m from the AZFP. Supercooling was calculated relative to the salinity- and pressure-dependent freezing point at 15 mBSL using potential temperature and salinity time-series at 75 m and 100 m depths respectively. This is achievable because of the remarkable homogeneity of the upper ocean for at least this depth range (Robinson et al., 2014), verified by oceanographic casts taken near the site sporadically throughout the deployments (Robinson et al., 2020a).

There are depths and times, such as around midnight on 6 November 2017, when there is negligible acoustic signal (i.e., signals < -100 dB shown in blue in Figures 1d) indicating that there are few scatterers in the water column. An optimization of such data attempts to characterize a scattering population, even though one probably does not exist. Therefore, we need to select appropriate S_v thresholds to identify physically realistic frazil populations. To demonstrate this process, optimized parameters for 5–9 November 2017 are combined in Figure 2, where they are further sorted into categories based on S_v at 200 kHz. There are noticeably different behaviors of population estimates depending on S_v, which are classified as either low ($S_v < -85\,\mathrm{dB}$), moderate ($-85\,\mathrm{dB} \leq S_v < -45\,\mathrm{dB}$) or high ($-45\,\mathrm{dB} \leq S_v$).

In general, the moderate scattering strengths lead to physically plausible population parameter estimates: the median size falls into the 0.1 mm to 1 mm range, and number densities are less than $10^5\,\mathrm{m}^{-3}$. In contrast, the parameter estimates of low and high scattering strength values often result in an unrealistically large number, e.g., $N > 10^{14}\ \mathrm{m}^{-3}$, of very small particles. From here onwards we focus solely on moderate scattering events.

The three parameters yielded by the optimization process, $\{\mu, \sigma, N\}$, are shown in Figures 3a-f. Implausible data are in grey. On the assumption that the scatterers are frazil ice crystals, the fractional ice volume, F, is calculated (see Supporting Information) and shown in Figures 4b and e, along with the tidal height (Figures 4a and d) and supercooling at 15 mBSL (Figure 4c and f). In 2017 current speed/direction (Figure 4g) at 100 mBSL is also shown.

As the 2017 deployment is closer to the ice shelf, we display the filtered population parameters, mean and standard deviation of D, and number density, N in Figure 5a-c. In order to obtain a characteristic estimate of a population of frazil crystals, the medians of filtered parameters are taken at 15 mBSL (white line in Figure 5a-c) in 2017 and found to be $\mu = -7.8$ and $\sigma = 1.3$. The log-normal distribution associated with these parameters is displayed in Figure 5d.

4 Discussion

It is likely that the filtered population of scatterers are frazil ice crystals because the derived fractional ice volume is correlated with supercooling, as demonstrated in Figure 5e at 15 mBSL. The fractional ice volume rises exponentially from $\sim 2 \times 10^{-6}$ to $\sim 8 \times 10^{-6}$ as supercooling increases 10 mK to 45 mK. In addition the supercooling behaves as expected for an ISW plume that is decaying with distance between sites at 13 km (in 2017) and 33 km (in 2016) from the ice shelf front: it hovered around $\sim$ 20 mK at the distant site, while on 6 November 2017 it rose to $\sim$ 40 mK at the site closer to the ice front. There the fractional ice volume is greatest ($\sim 10^{-5} - 10^{-4}$) at times following a tidal current from the direction of the ice shelf in the south east (compare Figures 1a, 4e & g). Consequently, the behaviour of all optimized parameters and the derived fractional ice volume (see Figures 1a, 3 & 4) is consistent with the interpretation of a mobile population of suspended frazil crystals of fractional ice volume up to 10^{-4}, being carried in a body of supercooled water underneath the sea ice. The magnitude of the fractional ice volume (Figures 4b & e) is consistent with observations in rivers (McFarlane et al., 2019).

River frazil diameters are known to be smaller during supercooling that is well established than during the time when supercooling is first imposed upon the water body (McFarlane et al., 2017, 2019). In the present case, the supercooling of the ISW plume has originated some distance from our sites, beneath the ice shelf, and is therefore well established. In addition, smaller crystal diameters are expected in salty ocean waters than in rivers (Schneck et al., 2019). Hence, the small value of the most frequently observed diameter of ocean frazil of 0.07 mm (see the mode of Figure 5d and Figure S2) might be expected. However the mean diameter derived for McMurdo Sound (1 mm in Figure 5d) is larger than in rivers and saline laboratory experiments ($\sim$0.5 mm in Schneck et al. (2019)). This can be explained by the large standard deviation in our observations (2.2 mm) that skews the McMurdo Sound distribution (see Figures 5d and S2). The broader sample distribution probably arises because crystals are more irregularly shaped in salt water than freshwater (Schneck et al., 2019), and because we are unable to distinguish individual crystals from flocs in our ISW plume observations.

In addition to comparison with previous results in rivers and laboratories, we assess the consistency of the derived fractional ice volume against other geophysical parameters. In November 2017 the sub-ice platelet layer was approximately 3.3 m thick, typical for a negative winter ocean heat flux between 30 and 35 $\mathrm{Wm^{-2}}$ (Langhorne et al., 2015) and locally equivalent to an ice accumulation of 8 – 10 mm per day. There are two contributions to the formation of this sub-ice platelet layer: (i) the tiny, suspended frazil crystals observed in the water column rise underneath the sea ice, and (ii) they grow larger in-situ at the ice–water interface, where the supercooling is greatest (Leonard et al., 2011; Mahoney et al., 2011; Robinson et al., 2014). We are unable to estimate the latter contribution, so we expect the accumulation of all suspended frazil to be less than 8 – 10 mm per day. For frazil crystals with diameters up to ∼1 mm, McFarlane et al. (2014) have observed rise velocities up to 9 $\mathrm{mms^{-1}}$, resulting in an accumulation (without in-situ growth) of 1 – 9 mm per day. This is of the same order, but less than, the value derived from the ocean heat flux. Hence the suspended frazil population parameters are consistent with other geophysical data.

Since we have a crystal size distribution, we can quantify the likelihood of small or large particles, e.g., $\mathrm{P}(D > 10\,\mathrm{mm}) \cong 0.01$, and hence substantiate the occasional observations of large crystals, even with size ∼25 mm (Penrose et al., 1994; Gough et al., 2012). Infrequent large crystals, such as those in the tail of Figure 5d, can have disproportionately large acoustic back-scattering, and scatter entirely outside the Rayleigh regime due to their size (Marko & Topham, 2015; Kungl et al., 2020).

Considerable frazil accumulation and growth were identified following periods of high scattering activity, both visually upon instrument retrieval and in the rising of the instrument from pressure records (e.g., Figure 1). This suggests an explanation for the horizontal striping that appears towards the end of deployments, and which gradually becomes more pronounced with time (Figures 1–4). We expect that this striping is related to ice attachment to the rope (Leonard et al., 2011; Robinson et al., 2014, 2020a) which, with continual growth, gradually enters the insonified volume of water. This assumption is supported by instrument rise after the development of these persistent scatterers in the 2017 deployments (e.g., November 13-14 in Figure 4e), indicating that a large volume of ice was accumulating on the AZFP and its mooring rope. However, in 2016 the instrument did not rise considerably due to its greater distance from the ice shelf front.

5 Conclusion

In this paper we provide observational data that constrain the frazil crystal population parameters under sea ice that have previously been unconstrained in models of ice shelf basal processes (Smedsrud & Jenkins, 2004; Hughes et al., 2014). To characterize frazil populations, in-situ acoustic and oceanographic data collected in an ISW plume under sea ice in McMurdo Sound for a total of 3 weeks in November 2016 and 2017 have been analyzed within a probabilistic framework based on an oblate spheroidal scattering model (Kungl et al., 2020). The parameters are estimated by an optimization routine comparing the scattering model to the acoustic observations at four frequencies (125, 200, 455, and 769 kHz). At distances between 13 and 33 km from the ice shelf front, and at a depth of 15 m below mean sea level, we have found $\sim 10^3 - 10^5$ crystals m^{-3} with a mean frazil diameter of approximately 1 mm, hence a fractional ice volume of $\sim 10^{-5}$. The frazil population parameters respond to the time-dependence of ocean currents and supercooling, with a demonstrated correlation between fractional ice volume and supercooling.

Acknowledgments

EKF, GHL, NJR and PJL have been supported by New Zealand's Deep South National Science Challenge, University of Otago, and the National Institute for Water and Atmospheric Research (NIWA). NJR is also grateful to the Marsden Fund. Logistical support was provided by Antarctica New Zealand and Dr T. Haskell of Callaghan Innovation and technical support from ASL Environmental Sciences. B. Grant, C. Stewart and P. de Joux of NIWA assisted with oceanographic data collection. DS acknowledges the financial support from the Dodd-Walls Centre for Photonics and Quantum Technologies. Acoustic and oceanographic data have been submitted to PANGAEA (www.pangaea.de) (Robinson et al., 2020b).

References

Brett, G. M., Irvin, A., Rack, W., Haas, C., Langhorne, P. J., & Leonard, G. H. (2020). Variability in the distribution of fast ice and the sub-ice platelet layer near mcmurdo ice shelf. *Journal of Geophysical Research: Oceans*, *125*(3), e2019JC015678. doi: 10.1029/2019JC015678

Daly, S. F. (1984). *Frazil ice dynamics* (Tech. Rep.). Cold Regions Research and Engineering Lab Hanover NH.

Dempsey, D. E., Langhorne, P. J., Robinson, N. J., Williams, M. J. M., Haskell, T. G., & Frew, R. D. (2010, jan). Observation and modeling of platelet ice fabric in McMurdo Sound, Antarctica. *Journal of Geophysical Research*, *115*(C1). doi: 10.1029/2008jc005264

Dieckmann, G., Rohardt, G., Hellmer, H., & Kipfstuhl, J. (1986, feb). The occurrence of ice platelets at 250 m depth near the Filchner Ice Shelf and its significance for sea ice biology. *Deep Sea Research Part A. Oceanographic Research Papers*, *33*(2), 141–148. doi: 10.1016/0198-0149(86)90114-7

Feistel, R. (2008). A Gibbs function for seawater thermodynamics for -6 to $80\,^{\circ}$c and salinity up to $120\,\mathrm{g\,kg^{-1}}$. *Deep Sea Research Part I: Oceanographic Research Papers*, *55*(12), 1639 - 1671. Retrieved from `http://www.sciencedirect.com/science/article/pii/S0967063708001489` doi: https://doi.org/10.1016/j.dsr.2008.07.004

Foldvik, A., & Kvinge, T. (1974, mar). Conditional instability of sea water at the freezing point. *Deep Sea Research and Oceanographic Abstracts*, *21*(3), 169–174. doi: 10.1016/0011-7471(74)90056-4

Frazer, E. (2019). *Characterising Frazil Ice Populations using Acoustic Techniques.* M. Sc. thesis, University of Otago.

Galton-Fenzi, B. K., Hunter, J. R., Coleman, R., Marsland, S. J., & Warner, R. C. (2012). Modeling the basal melting and marine ice accretion of the amery ice shelf. *Journal of Geophysical Research: Oceans*, *117*(C9). doi: 10.1029/2012JC008214

Ghobrial, T. R., Loewen, M. R., & Hicks, F. E. (2013). Characterizing suspended frazil ice in rivers using upward looking sonars. *Cold Regions Science and Technology*, *86*, 113–126.

Gough, A. J., Mahoney, A. R., Langhorne, P. J., Williams, M. J., Robinson, N. J.,

& Haskell, T. G. (2012). Signatures of supercooling: McMurdo Sound platelet ice. *Journal of Glaciology*, *58*(207), 38–50. doi: 10.3189/2012JoG10J218

Holland, P. R., & Feltham, D. L. (2005, may). Frazil dynamics and precipitation in a water column with depth-dependent supercooling. *Journal of Fluid Mechanics*, *530*, 101–124. doi: 10.1017/s002211200400285x

Hughes, K. G., Langhorne, P. J., Leonard, G. H., & Stevens, C. L. (2014, dec). Extension of an Ice Shelf Water plume model beneath sea ice with application in McMurdo Sound, Antarctica. *Journal of Geophysical Research: Oceans*, *119*(12), 8662–8687. doi: 10.1002/2013jc009411

Ito, M., Fukamachi, Y., Ohshima, K. I., & Shirasawa, K. (2020). Observational evidence of supercooling and frazil ice formation throughout the water column in a coastal polynya in the Sea of Okhotsk. *Continental Shelf Research*, *196*, 104072. doi: https://doi.org/10.1016/j.csr.2020.104072

Ito, M., Ohshima, K. I., Fukamachi, Y., Mizuta, G., Kusumoto, Y., & Nishioka, J. (2017). Observations of frazil ice formation and upward sediment transport in the Sea of Okhotsk: A possible mechanism of iron supply to sea ice. *Journal of Geophysical Research: Oceans*, *122*(2), 788-802. doi: 10.1002/2016JC012198

Ito, M., Ohshima, K. I., Fukamachi, Y., Simizu, D., Iwamoto, K., Matsumura, Y., ... Eicken, H. (2015). Observations of supercooled water and frazil ice formation in an Arctic coastal polynya from moorings and satellite imagery. *Annals of Glaciology*, *56*(69), 307–314. doi: 10.3189/2015aog69a839

Jenkins, A., & Bombosch, A. (1995). Modeling the effects of frazil ice crystals on the dynamics and thermodynamics of Ice Shelf Water plumes. *Journal of Geophysical Research*, *100*(C4), 6967. doi: 10.1029/94jc03227

Kungl, A. F., Schumayer, D., Frazer, E. K., Langhorne, P. J., & Leonard, G. H. (2020). An oblate spheroidal model for multi-frequency acoustic backscattering of frazil ice. *Cold Regions Science and Technology*, *177*, 103122. doi: https://doi.org/10.1016/j.coldregions.2020.103122

Langhorne, P. J., Hughes, K. G., Gough, A. J., Smith, I. J., Williams, M. J. M., Robinson, N. J., ... Haskell, T. G. (2015, jul). Observed platelet ice distributions in Antarctic sea ice: An index for ocean-ice shelf heat flux. *Geophysical Research Letters*, *42*(13), 5442–5451. doi: 10.1002/2015gl064508

Leonard, G. H., Langhorne, P. J., Williams, M. J. M., Vennell, R., Purdie, C. R., Dempsey, D. E., … Frew, R. D. (2011, apr). Evolution of supercooling under coastal Antarctic sea ice during winter. *Antarctic Science*, *23*(04), 399–409. doi: 10.1017/s0954102011000265

Leonard, G. H., Purdie, C. R., Langhorne, P. J., Haskell, T. G., Williams, M. J. M., & Frew, R. D. (2006). Observations of platelet ice growth and oceanographic conditions during the winter of 2003 in McMurdo Sound, Antarctica. *Journal of Geophysical Research*, *111*(C4). doi: 10.1029/2005jc002952

Lewis, E. L., & Perkin, R. G. (1985). The winter oceanography of McMurdo Sound, Antarctica. In *Oceanology of the Antarctic Continental Shelf* (pp. 145–165). American Geophysical Union. doi: 10.1029/ar043p0145

Lewis, E. L., & Perkin, R. G. (1986). Ice pumps and their rates. *Journal of Geophysical Research*, *91*(C10), 11756. doi: 10.1029/jc091ic10p11756

MacAyeal, D. R. (1984). Thermohaline circulation below the Ross Ice Shelf: A consequence of tidally induced vertical mixing and basal melting. *Journal of Geophysical Research*, *89*(C1), 597. doi: 10.1029/jc089ic01p00597

Mahoney, A. R., Gough, A. J., Langhorne, P. J., Robinson, N. J., Stevens, C. L., Williams, M. M. J., & Haskell, T. G. (2011, nov). The seasonal appearance of ice shelf water in coastal Antarctica and its effect on sea ice growth. *Journal of Geophysical Research*, *116*(C11). doi: 10.1029/2011jc007060

Marko, J. R., & Jasek, M. (2010). Sonar detection and measurements of ice in a freezing river I: Methods and data characteristics. *Cold Regions Science and Technology*, *63*(3), 121–134.

Marko, J. R., Jasek, M., & Topham, D. R. (2015, feb). Multifrequency analyses of 2011–2012 Peace River SWIPS frazil backscattering data. *Cold Regions Science and Technology*, *110*, 102–119. doi: 10.1016/j.coldregions.2014.11.006

Marko, J. R., & Topham, D. R. (2015, April). Laboratory measurements of acoustic backscattering from polystyrene pseudo-ice particles as a basis for quantitative characterization of frazil ice. *Cold Regions Science and Technology*, *112*, 66–86. doi: 10.1016/j.coldregions.2015.01.003

Martin, S. (1981). Frazil ice in rivers and oceans. *Annual Review of Fluid Mechanics*, *13*(1), 379–397.

McDougall, T. (2011). *Getting started with TEOS-10 and the Gibbs seawater (GSW) Oceanographic Toolbox*. Battery Point, Tas: Trevor J McDougall.

McFarlane, V., Loewen, M., & Hicks, F. (2014, oct). Laboratory measurements of the rise velocity of frazil ice particles. *Cold Regions Science and Technology*, *106-107*, 120–130. doi: 10.1016/j.coldregions.2014.06.009

McFarlane, V., Loewen, M., & Hicks, F. (2015). Measurements of the evolution of frazil ice particle size distributions. *Cold Regions Science and Technology*, *120*, 45 - 55. Retrieved from `http://www.sciencedirect.com/science/article/pii/S0165232X1500186X` doi: https://doi.org/10.1016/j.coldregions.2015.09.001

McFarlane, V., Loewen, M., & Hicks, F. (2017, October). Measurements of the size distribution of frazil ice particles in three Alberta rivers. *Cold Regions Science and Technology*, *142*, 100–117. doi: 10.1016/j.coldregions.2017.08.001

McFarlane, V., Loewen, M., & Hicks, F. (2019). Field measurements of suspended frazil ice. part ii: Observations and analyses of frazil ice properties during the principal and residual supercooling phases. *Cold Regions Science and Technology*, *165*, 102796. doi: https://doi.org/10.1016/j.coldregions.2019.102796

Penrose, J. D., Conde, M., & Pauly, T. J. (1994). Acoustic detection of ice crystals in Antarctic waters. *Journal of Geophysical Research*, *99*(C6), 12573. doi: 10.1029/93jc03507

Rees Jones, D. W., & Wells, A. J. (2018). Frazil-ice growth rate and dynamics in mixed layers and sub-ice-shelf plumes. *The Cryosphere*, *12*(1), 25–38. Retrieved from `https://tc.copernicus.org/articles/12/25/2018/` doi: 10.5194/tc-12-25-2018

Richard, M., Morse, B., Daly, S. F., & Emond, J. (2011). Quantifying suspended frazil ice using multi-frequency underwater acoustic devices. *River Research and Applications*, *27*(9), 1106–1117.

Robinson, N. J., Grant, B., Stevens, C., Stewart, C., & Williams, M. (2020a). Oceanographic observations in supercooled water: Protocols for mitigation of measurement errors in profiling and moored sampling. *Cold Regions Science and Technology*, *170*, 102954. doi: https://doi.org/10.1016/j.coldregions.2019.102954

Robinson, N. J., Leonard, G., Frazer, E., Langhorne, P., Grant, B., Stewart, C., & De Joux, P. (2020b). Temperature, salinity and acoustic backscatter observations and tidal model output in McMurdo Sound, Antarctica in 2016 and 2017.

In *Pangaea Data Archiving.* Alfred Wegener Institute, Helmholtz Centre for Polar and Marine Research. doi: pending

Robinson, N. J., Williams, M. J. M., Stevens, C. L., Langhorne, P. J., & Haskell, T. G. (2014). Evolution of a supercooled Ice Shelf Water plume with an actively growing subice platelet matrix. *Journal of Geophysical Research: Oceans*, *119*(6), 3425–3446.

Schneck, C. C., Ghobrial, T. R., & Loewen, M. R. (2019). Laboratory study of the properties of frazil ice particles and flocs in water of different salinities. *The Cryosphere*, *13*(10), 2751–2769. doi: 10.5194/tc-13-2751-2019

Smedsrud, L. H. (2001). Frazil-ice entrainment of sediment: large-tank laboratory experiments. *Journal of Glaciology*, *47*(158), 461471. doi: 10.3189/172756501781832142

Smedsrud, L. H., & Jenkins, A. (2004, mar). Frazil ice formation in an ice shelf water plume. *Journal of Geophysical Research: Oceans*, *109*(C3). doi: 10.1029/2003jc001851

Svensson, U., & Omstedt, A. (1998). Numerical simulations of frazil ice dynamics in the upper layers of the ocean. *Cold Regions Science and Technology*, *28*(1), 29 - 44. doi: https://doi.org/10.1016/S0165-232X(98)00011-1

Tsang, G., & Hanley, T. O. (1985). Frazil formation in water of different salinities and supercoolings. *Journal of Glaciology*, *31*(108), 7485. doi: 10.3189/S0022143000006298

6 Figures

Figure 1. (a) Map with 2016 and 2017 sites. (b) Vertical profile taken at 5:59PM on 11 November, 2017 (shown by dashed line in panel d). (c-d) Scattering strength, S_v [dB], of 200 kHz channel deployments plotted against date in November 2016 and 2017, respectively. Black represents bins that were not insonified, either because the instrument was too high in the water column or it had been taken out to remove ice accumulation. Horizontal white line indicates 15 mBSL reference depth.

Figure 2. (a) Three categories of back-scattering strength, S_v, shown for the 200 kHz channel, 5–9 November 2017: low (blue, $S_v < -85\,\mathrm{dB}$), moderate (orange, $-85\,\mathrm{dB} \leq S_v < -45\,\mathrm{dB}$) and high (yellow, $-45\,\mathrm{dB} \leq S_v$). The three remaining subplots depict the corresponding log-normal parameter distributions: (b) σ, (c) $\mu_{10} = \log_{10}(\exp(\mu))$, and (d) $\log_{10} N$.

Figure 3. Optimized parameters, $\{\mu, \sigma, N\}$, plotted against days in November 2016 (a, c and e) and November 2017 (b, d and f) respectively. $\mu_{10} = \log_{10}(\exp(\mu))$ and σ are standard parameters of the log-normal distribution in base 10, while $\log_{10}(N)$ is the number density of crystals per unit volume. Black means 'not insonified', grey 'outside S_v thresholds'.

Figure 4. Tidal height (a & d), fractional ice volume (b & e), supercooling at 15 mBSL, calculated from deeper temperature and salinity records (c & f), plotted against day in November 2016 and 2017, respectively. Black not insonified, grey outside S_v thresholds. (g) Current speed/direction at 100 mBSL in 2017, with north to top of page and length of arrow representing speed.

Figure 5. Filtered population parameters calculated from the moderate scattering events and plotted against days in November 2017: (a) mean frazil diameter, D [mm], (b) standard deviation of D [mm], and (c) number density, $\log_{10}(N)$ [m^{-3}]. Black not insonified, grey outside S_v thresholds. (d) Log-normal population density function using the mean parameter values at 15 mBSL in 2017 (median(μ) $= -7.8$ and median(σ) $= 1.3$). The blue dashed line indicates the median frazil diameter (≈ 0.4 mm), while the red dash-dotted line represents the mean frazil diameter (≈ 1.0 mm). Inset depicts the same information over a logarithmic abscissa. (e) Fractional ice volume, F, plotted against supercooling at 15 mBSL, with fitted line (in red).

Figure 1.

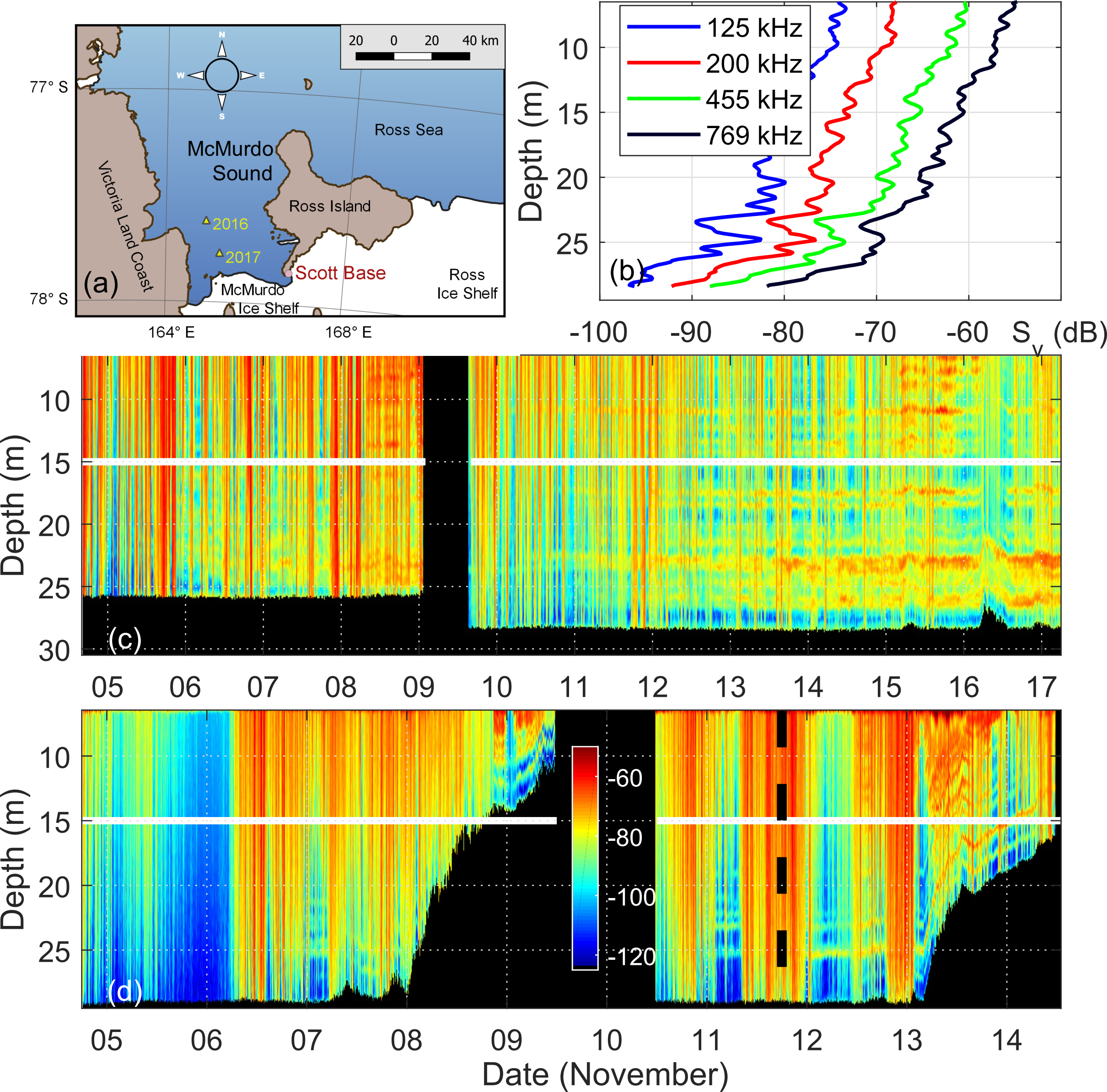

20 0 20 40 km
N
W
E
S
77° S
78° S
164° E
168° E
McMurdo Sound
Ross Sea
Ross Island
Victoria Land Coast
2016
2017
Scott Base
McMurdo Ice Shelf
Ross Ice Shelf
(a)
125 kHz
200 kHz
455 kHz
769 kHz
Depth (m)
(b)
-100 -90 -80 -70 -60 S_v (dB)
(c)
05 06 07 08 09 10 11 12 13 14 15 16 17
-60
-80
-100
-120
(d)
05 06 07 08 09 10 11 12 13 14
Date (November)

Figure 2.

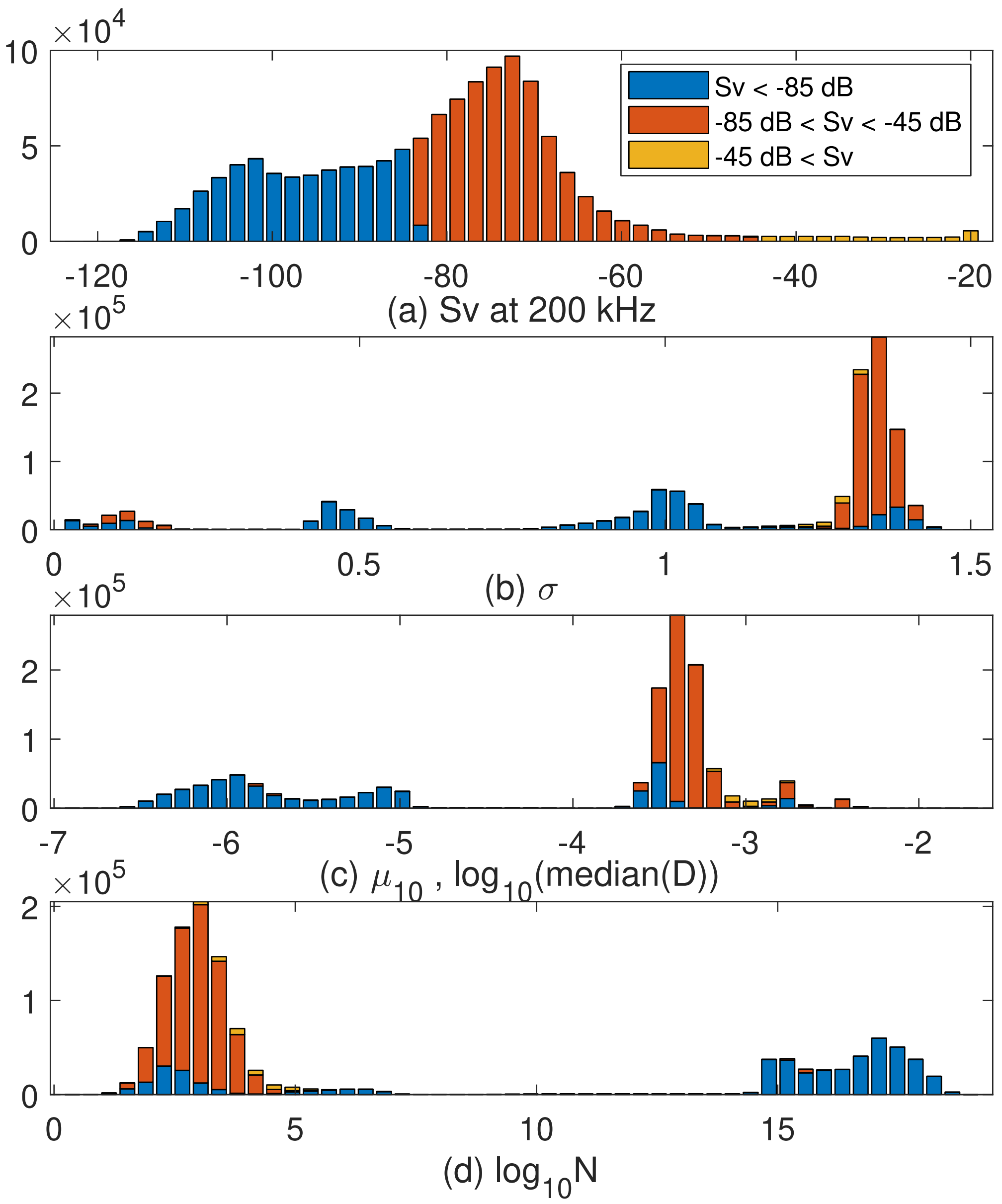

×10^4
Sv < -85 dB
-85 dB < Sv < -45 dB
-45 dB < Sv
(a) Sv at 200 kHz
×10^5
(b) σ
×10^5
(c) μ10 , log10(median(D))
×10^5
(d) log10N

Figure 3.

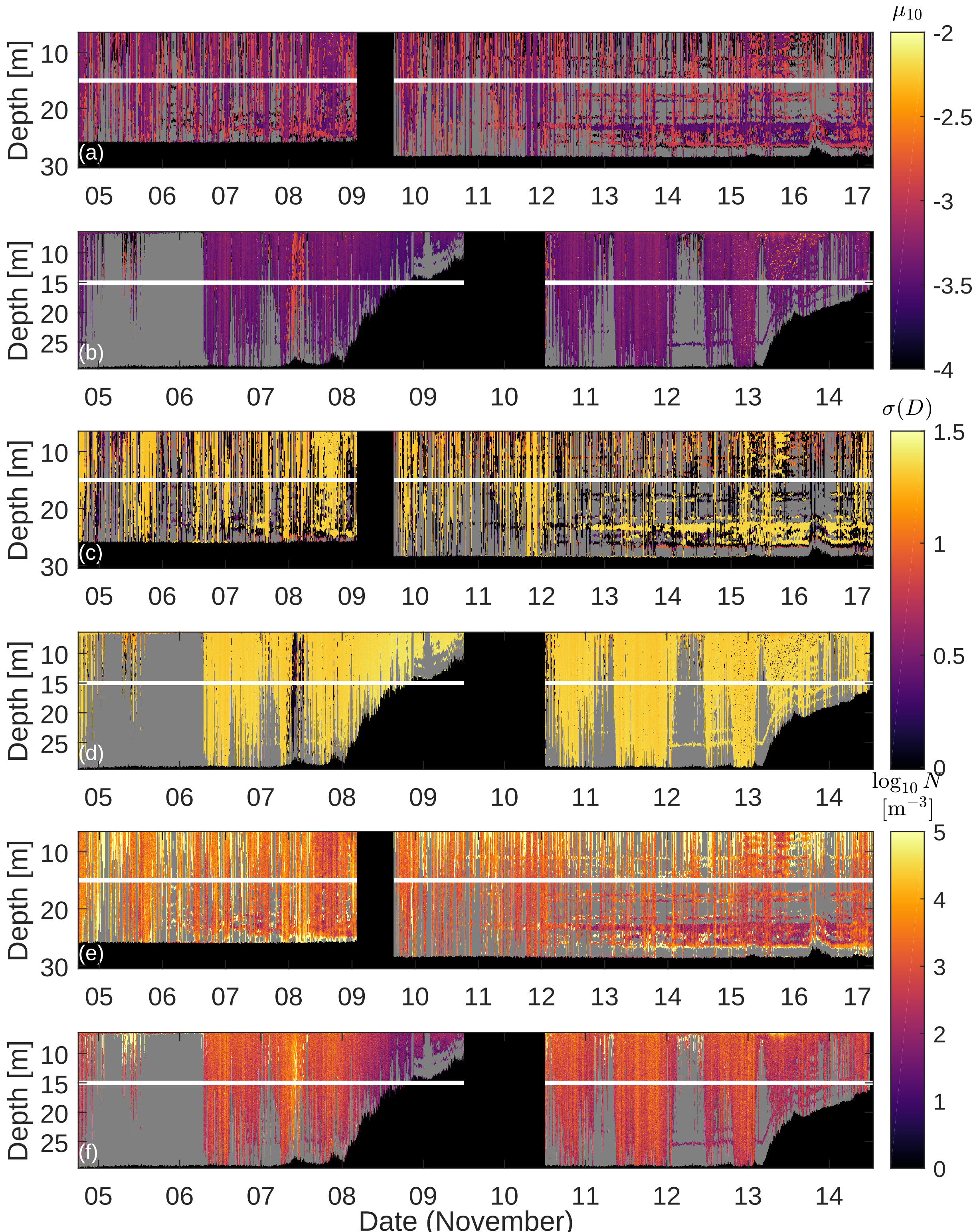

μ_{10}
$\sigma(D)$
$\log_{10} N$ $[\mathrm{m}^{-3}]$
Depth [m]
(a)
(b)
(c)
(d)
(e)
(f)
Date (November)

Figure 4.

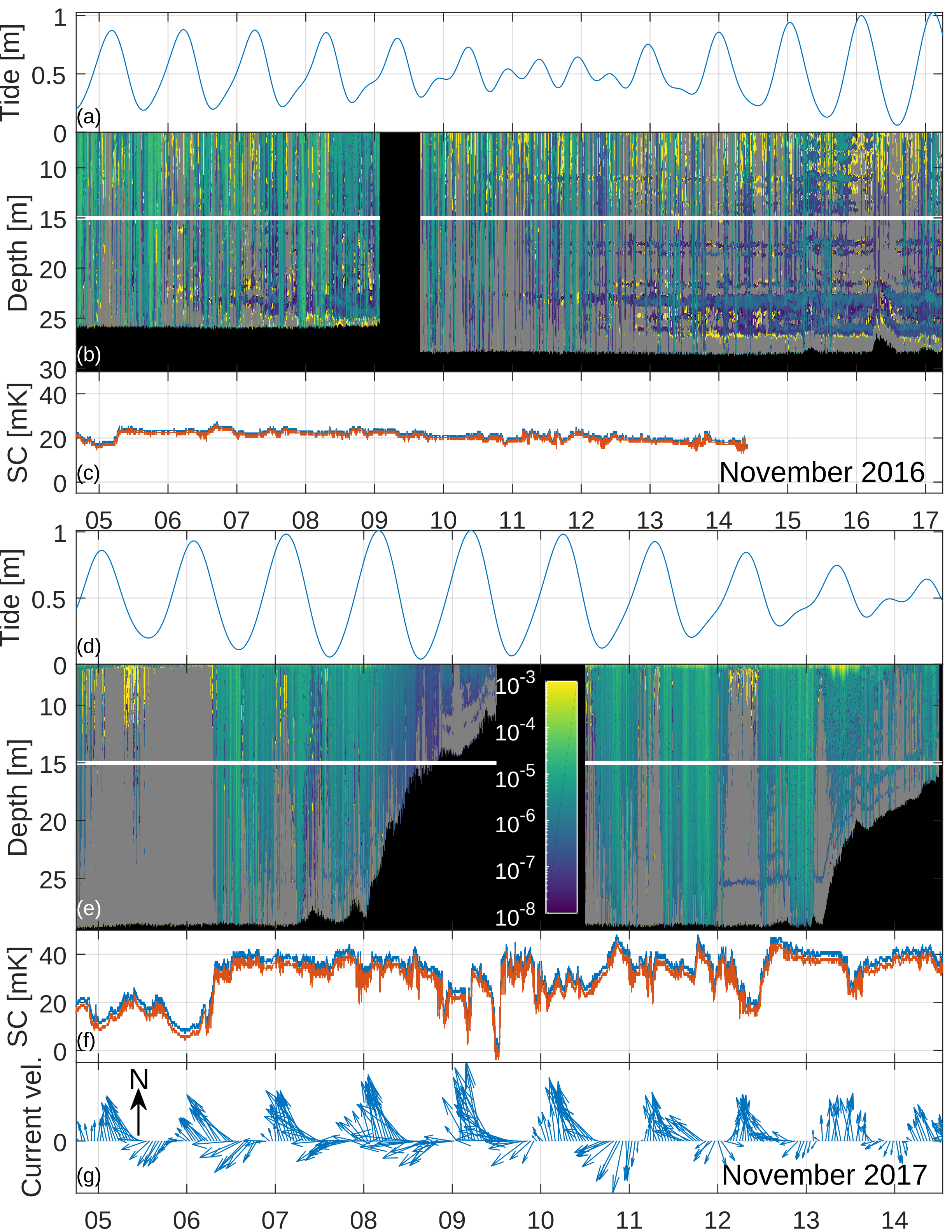

Tide [m]
(a)
Depth [m]
(b)
SC [mK]
(c)
November 2016
05 06 07 08 09 10 11 12 13 14 15 16 17
Tide [m]
(d)
Depth [m]
(e)
10^-3 10^-4 10^-5 10^-6 10^-7 10^-8
SC [mK]
(f)
Current vel.
N
(g)
November 2017
05 06 07 08 09 10 11 12 13 14

Figure 5.

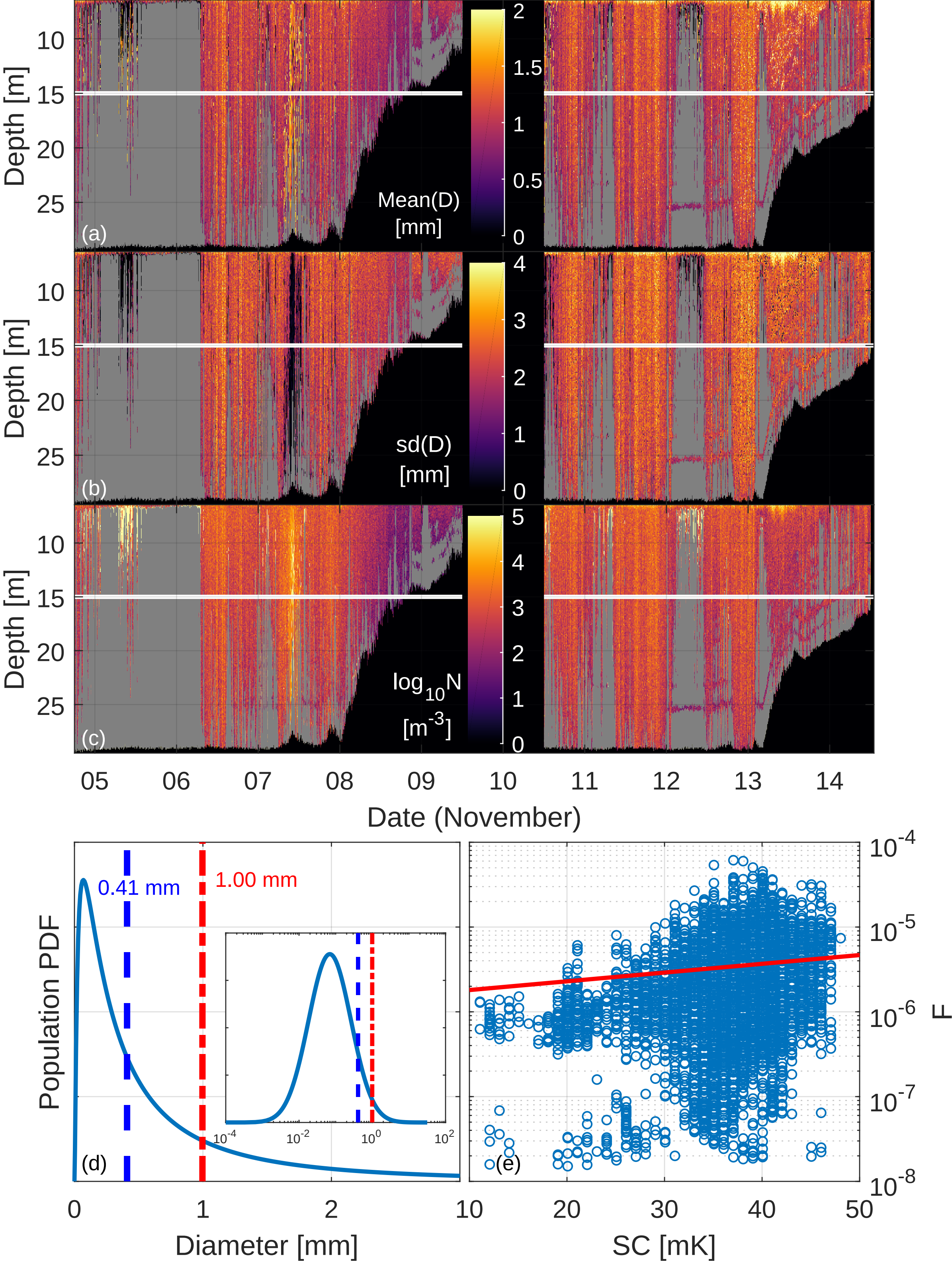

Depth [m]
Mean(D) [mm]
(a)
sd(D) [mm]
(b)
$\log_{10}N$ [m^{-3}]
(c)
Date (November)
05 06 07 08 09 10 11 12 13 14
Population PDF
0.41 mm
1.00 mm
(d)
Diameter [mm]
(e)
SC [mK]
F

Supporting Information for "Observations of the size distribution of frazil ice in an Ice Shelf Water plume"

Eamon K. Frazer[1], Pat J. Langhorne[1], Greg H. Leonard[2], Natalie J. Robinson[3], Dániel Schumayer[1,4]

[1]Department of Physics, University of Otago, Dunedin, New Zealand

[2]School of Surveying, University of Otago, Dunedin, New Zealand

[3]National Institute of Water and Atmospheric Research, Wellington, New Zealand

[4]The Dodd-Walls Centre for Photonic and Quantum Technologies, Dunedin, New Zealand

Contents of this file

Description of the AZFP

The AZFP profiles the water column by pulsing acoustic waves at four frequencies (125 kHz, 200 kHz, 455 kHz, and 769 kHz) using four separate monostatic transducers and receivers. The acoustic backscatter is recorded by the instrument and converted to a volume backscatter strength. Ten profiles were collected at each sampling interval and then averaged. Samples were undertaken at 1 minute intervals. The ASL Matlab Toolbox (version 1.1) was used to convert raw instrument counts to acoustic volume backscattering strength, S_v, related to the back-scattering cross section, $\Sigma_{\rm bs}^{\rm obs}$.

The S_v data are taken as a time series at fixed ranges in each deployment, such that they remain roughly equidistant from the ice-ocean interface over time. Data are measured in 0.1 m vertical cells, then spatially averaged over 0.5 m centered on the depth specified in the analysis. The resulting spatially-averaged time series is smoothed using MATLAB's `rlowess` algorithm, a 1st degree polynomial model with linear least square fitting. This process is repeated for all depths of interest in the water column, from the ice-ocean interface down to ≈2m from the AZFP. This range excludes the bulk of the ice layer and the portion of the water column affected by the near-field interference of the sonar.

Further details of the instrumentation and its mode of deployment are available in Kungl et al. (2020), Frazer (2019) and in the metadata files of Robinson et al. (2020b).

Details of data analysis

An overview of the data processing is shown in Figure S1.

The total back-scattering cross-section, $\Sigma_{\rm bs}^{\rm th}(\nu)$, at frequency ν for a dilute population of scatterers with random diameter D can be modeled by

$$\Sigma_{\rm bs}^{\rm th}(\nu) = N \int g(D)\, \sigma_{\rm bs}(\nu, D)\, dD, \qquad (1)$$

where $\Sigma_{\rm bs}^{\rm th}(\nu)$ is the ratio of back-scattered intensity from a unit volume of 1m^3 to the intensity of the incident plane wave (referenced to 1m), N is the number density of scatterers, $\sigma_{\rm bs}$ is the scattering cross-section of a single obstacle, and g is a probability distribution of scatterers' diameter (Marko & Jasek, 2010). Below we model g and $\sigma_{\rm bs}$, and identify the left-hand side of this equation with the measured back-scattering cross-section $\Sigma_{\rm bs}^{\rm obs}(\nu)$, noting that

$$S^{\rm obs} = 10 \log_{10}(\Sigma_{\rm bs}^{\rm obs}) \quad \text{and} \quad S^{\rm th} = 10 \log_{10}(\Sigma_{\rm bs}^{\rm th}).$$

Recent observations (Marko et al., 2015; McFarlane et al., 2017, 2019; Schneck et al., 2019) and theoretical considerations (Crow & Shimizu, 1988) recommend choosing a log-normal distribution for g. This probability distribution is governed by a location and a scale parameter, μ and σ. Parameters μ and σ are the mean and standard deviation of the transformed random variable $\ln(D)$, where ln() denotes the natural logarithm. The physically important statistical moments of D are

$$\begin{aligned} \text{median}(D) &= \exp(\mu), \\ \text{mean}(D) &= \exp(\mu + \tfrac{1}{2}\sigma^2), \\ \text{mode}(D) &= \exp(\mu - \sigma^2), \quad \text{and} \\ \text{variance}(D) &= \left[\exp(\sigma^2) - 1\right] \exp(2\mu + \sigma^2) \end{aligned}$$

Assuming low scatterer number and a uniformly random orientation of crystals, we have provided an analytic expression for the back-scattering cross-section $\sigma_{\rm bs}$ of an individual crystal modeled as an oblate spheroid (Kungl et al., 2020).

Although g depends on yet unknown parameters, and $\sigma_{\rm bs}$ is expressed in terms of a random variable D and known frequencies, the integral (1) can be determined either analytically or numerically for any given set of $\{\mu, \sigma, N\}$. Thus there are three unknown quantities and four measurement channels at a given depth and given time, hence the mathematical problem is over-determined assuming perfect observation. However, since observed data are encumbered with noise from different sources, it is more natural to re-interpret the task of determining $\{\mu, \sigma, N\}$ as an optimization problem. We seek the parameter values that optimally approximate the observed back-scattering cross-sections, $\Sigma_{\rm bs}^{\rm obs}$, provided by observation. The goodness-of-fit is measured by the standard residual sum of squares

$$R = \sum_{i=1}^{4} \Big[S^{\rm th}(\nu_i) - S^{\rm obs}(\nu_i) \Big]^2.$$

In order to limit R to $\sim$ 1dB (similar to the uncertainty of the instrument) some constraints are placed on the parameter space to avoid non-physical solutions. An upper bound is put on the total fractional ice volume, F, defined as the volume of ice per cubic meter of ocean

$$F = N \int g(D)\, V(D, \tau)\, dD = \frac{\pi}{6} N\tau \exp\left(3\mu + \tfrac{9}{2}\sigma^2\right), \qquad (2)$$

0094-8276/20/$5.00

where $V(D,\tau) = \frac{\pi}{6}D^3\tau$ is the volume of a single oblate spheroidal crystal of diameter D and thickness ratio τ. In this work we use $\tau = 1/30$ (Dempsey et al., 2010; McFarlane et al., 2012, 2014; Kungl et al., 2020) and employed the numerical constraint, $F < 10^{-1}$. This constraint is quite permissive, much higher than expected values in the ocean (Penrose et al., 1994). For the nonlinear constrained optimization we used Matlab's built-in interior-point algorithm, `fmincon`. The optimization procedure terminates if

1. R has reached its minimum at a tolerance of 10^{-6}, and
2. F does not change by more than 10^{-12}.

The same process (see Figure S1) is repeated for the entire time-series.

Notes on data filtering

Removal of data with $S^{\mathrm{obs}} > -45\,\mathrm{dB}$ value can be justified because such signals are present at all frequencies indicating large scatterers. Most likely signals are from the bottom of the sub-ice platelet layer or perhaps due to occasional large marine life.

The bimodality of the distribution of S_v in Figure 2a of the main manuscript suggested that there could be two (or more) distinct cohort of scatterers. That histogram represents the 200 kHz channel of the dataset taken 5–9 November 2017. Therefore we chose to fit two Gaussian distributions to this histogram and obtained mean and standard deviations of $(\mu_1, \sigma_1) = (-101.00, 10.96)\,\mathrm{dB}$ and $(\mu_2, \sigma_2) = (-75.00, 7.23)\,\mathrm{dB}$. From these parameters we select a cut-off value in the range $(-90, -83)\,\mathrm{dB}$.

Unlike the oblate spheroidal scattering model, or the optimization algorithm, this choice was heuristic. Consequently we repeated the optimization algorithm calculation for a few cut-off values in this range. These optimization runs all led to similar $\{\mu_{10}, \sigma, N\}$ results. Hence we concluded that the optimization was not sensitive to the precise value of the cut-off value of $-85\,\mathrm{dB}$. It is apparent from Figure 2b-d of the main text that the blue and orange data points, determined by their S_v values, do represent physically distinct groups of $\{\mu_{10}, \sigma, N\}$ parameters and the cohort colored blue corresponds to very large number of extremely small particles, which –on physical grounds– we managed to exclude from any analysis by imposing the cut-off values on the S_v data.

Two remarks are due here.

(i) In selecting the 200 kHz channel for determining the cut-off value we considered two counteracting arguments. First, we wanted to select a channel which is the 'loudest', i.e., has the highest frequency, as it picks up more features in the insonified volume. On the other hand we wanted a channel which is insensitive against details our model does not contain. This second consideration means that we wish all scatterers to scatter within the Rayleigh regime, i.e., the frequency cannot be too high. Thus we opt for the 200 kHz channel.

(ii) While not all deployments and all channels show such clear bimodality, we checked the 200 kHz channel of other deployments and fitted a mixture of two Gaussians on these histograms too. Those transition ranges did contain the $-85\,\mathrm{dB}$ value.

Comparison with salt water laboratory studies

Figure S2 shows the log-normal population density function using the mean parameter values at 15 mBSL in 2017 in comparison to the frazil ice distributions in saline water of 35 ppt found by Schneck et al. (2019). Distribution mean, standard deviation, and mode are shown. The larger standard deviation of the present work probably arises because we are unable to separate individual crystals from flocs as has been done by Schneck et al. (2019).

References

Crow, E. L., & Shimizu, K. (1988). *Lognormal distributions: theory and applications* (E. L. Crow & K. Shimizu, Eds.). New York: M. Dekker.

Dempsey, D. E., Langhorne, P. J., Robinson, N. J., Williams, M. J. M., Haskell, T. G., & Frew, R. D. (2010, jan). Observation and modeling of platelet ice fabric in McMurdo Sound, Antarctica. *Journal of Geophysical Research*, *115*(C1). doi: 10.1029/2008jc005264

Frazer, E. (2019). *Characterising Frazil Ice Populations using Acoustic Techniques* (M. Sc. thesis). University of Otago.

Kungl, A. F., Schumayer, D., Frazer, E. K., Langhorne, P. J., & Leonard, G. H. (2020). An oblate spheroidal model for multi-frequency acoustic back-scattering of frazil ice. *Cold Regions Science and Technology*, *177*, 103122. doi: https://doi.org/10.1016/j.coldregions.2020.103122

Marko, J. R., & Jasek, M. (2010). Sonar detection and measurements of ice in a freezing river I: Methods and data characteristics. *Cold Regions Science and Technology*, *63*(3), 121–134.

Marko, J. R., Jasek, M., & Topham, D. R. (2015, feb). Multifrequency analyses of 2011–2012 Peace River SWIPS frazil backscattering data. *Cold Regions Science and Technology*, *110*, 102–119. doi: 10.1016/j.coldregions.2014.11.006

McFarlane, V., Loewen, M., & Hicks, F. (2012). Laboratory experiments to determine frazil ice properties. In *Proceedings of the Annual General Conference of the Canadian Society of Civil Engineers, Edmonton, Alberta, Canada, June* (Vol. 6).

McFarlane, V., Loewen, M., & Hicks, F. (2014, oct). Laboratory measurements of the rise velocity of frazil ice particles. *Cold Regions Science and Technology*, *106-107*, 120–130. doi: 10.1016/j.coldregions.2014.06.009

McFarlane, V., Loewen, M., & Hicks, F. (2017, October). Measurements of the size distribution of frazil ice particles in three Alberta rivers. *Cold Regions Science and Technology*, *142*, 100–117. doi: 10.1016/j.coldregions.2017.08.001

McFarlane, V., Loewen, M., & Hicks, F. (2019). Field measurements of suspended frazil ice. part ii: Observations and analyses of frazil ice properties during the principal and residual supercooling phases. *Cold Regions Science and Technology*, *165*, 102796. doi: https://doi.org/10.1016/j.coldregions.2019.102796

Penrose, J. D., Conde, M., & Pauly, T. J. (1994). Acoustic detection of ice crystals in Antarctic waters. *Journal of Geophysical Research*, *99*(C6), 12573. doi: 10.1029/93jc03507

Robinson, N. J., Leonard, G., Frazer, E., Langhorne, P., Grant, B., Stewart, C., & De Joux, P. (2020b). Temperature, salinity and acoustic backscatter observations and tidal model output in McMurdo Sound, Antarctica in 2016 and 2017. In *Pangaea Data Archiving.* Alfred Wegener Institute, Helmholtz Centre for Polar and Marine Research. doi: pending

Schneck, C. C., Ghobrial, T. R., & Loewen, M. R. (2019). Laboratory study of the properties of frazil ice particles and flocs in water of different salinities. *The Cryosphere*, *13*(10), 2751–2769. doi: 10.5194/tc-13-2751-2019

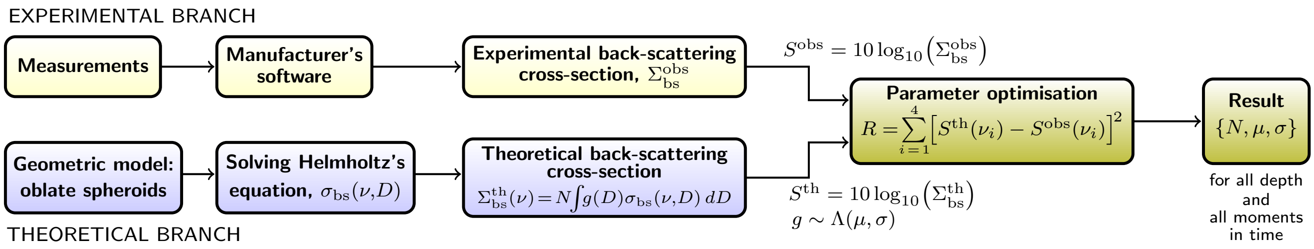

Figure S1. The flow diagram shows how the experimental and data preparation and the theoretical modeling are combined in a classical optimization process to obtain estimates of $\{N, \mu, \sigma\}$. Here N denotes the number of frazil crystals in the insonified volume at a given depth and a fixed moment in time. Parameters μ and σ characterize the log-normal probability distribution $g \sim \Lambda(\mu, \sigma)$ describing the likelihood observing an oblate spheroid of size D.

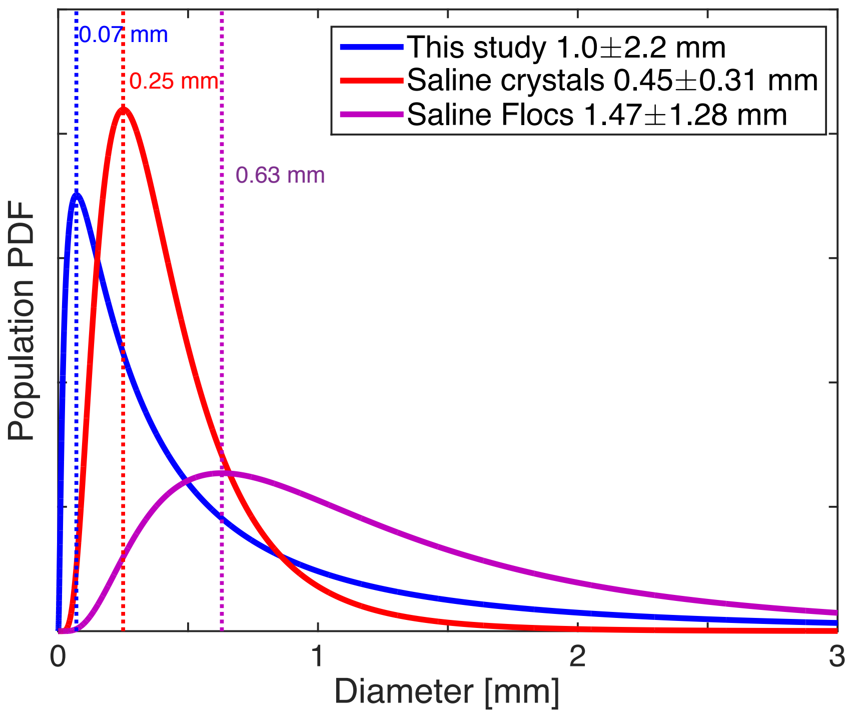

Figure S2. Comparison of present distribution (in blue) with that of salt water experiments at 35 ppt of Schneck et al. (2019), with individual frazil ice crystals in red and frazil flocs in magenta. The arithmetic mean and standard deviation of each distribution is shown in the legend. The modes (the most likely values of the distribution) are shown by vertical dotted lines and color-coded.